

This is the preprint of the contribution published as:

Hu, J., **Zhang, H.**, Xia, S., Cai, Y., Shi, Z., Deng, J. (2026):
Harnessing the Co-Fe synergy: A novel Co-doped FeOCl for peracetic acid activation to
efficiently degrade carbamazepine
Colloid Surf. A-Physicochem. Eng. Asp. **742, Part 1** , art. 140410

The publisher's version is available at:

<https://doi.org/10.1016/j.colsurfa.2026.140410>

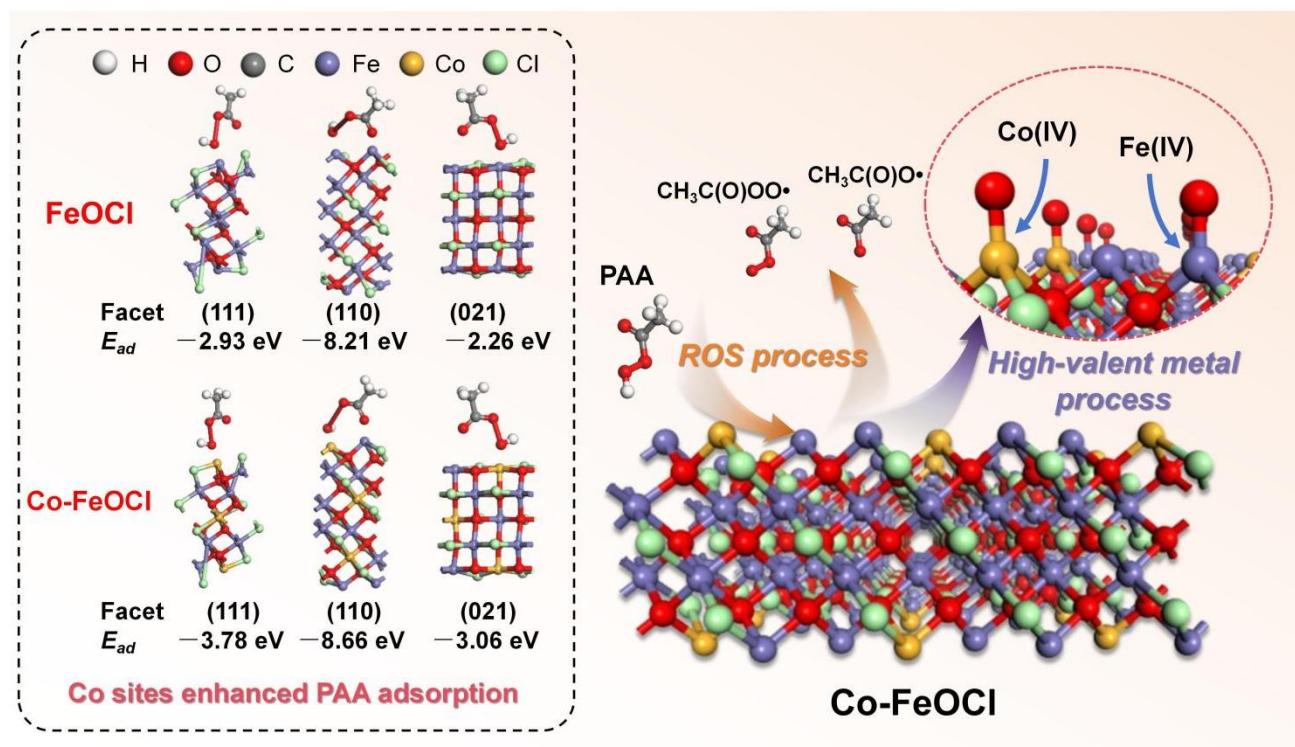
Colloids and Surfaces A: Physicochemical and Engineering Aspects

Cobalt-doped FeOCl for peracetic acid activation toward carbamazepine degradation: Crystal facet regulation and Co–Fe synergy

--Manuscript Draft--

Manuscript Number:	
Article Type:	Research Paper
Keywords:	Co-doped FeOCl; Peracetic acid; Carbamazepine degradation; Advanced oxidation processes; Synergistic mechanism
Corresponding Author:	Haojie Zhang Hunan University CHINA
First Author:	Jinlin Hu
Order of Authors:	Jinlin Hu Haojie Zhang Simeng Xia Zhou Shi Lin Deng
Abstract:	<p>The widespread occurrence of carbamazepine (CBZ) in aquatic environments necessitates efficient water treatment technologies. This study developed a cobalt-doped iron oxychloride (Co-FeOCl) catalyst via a facile calcination method to activate peracetic acid (PAA) for enhanced degradation of CBZ. The incorporation of Co into the FeOCl structure dramatically boosted the catalytic performance, with 0.5Co-FeOCl exhibiting superior activity compared to pristine FeOCl. The 0.5Co-FeOCl/PAA system achieved an apparent rate constant of 0.039 min⁻¹, 19.5 and 5.6 times higher than that of the PAA alone (0.002 min⁻¹) and FeOCl/PAA (0.007 min⁻¹) systems, respectively. Mechanistic investigations revealed that the degradation was primarily driven by organic radicals (CH₃C(O)OO• and CH₃C(O)O•) and high-valent metal species (Co(IV) and Fe(IV)). The Co doping established synergistic Fe(II)/Fe(III)-Co(II)/Co(III) redox cycles, effectively accelerating the rate-limiting Fe(III) reduction step and facilitating continuous generation of reactive species. XPS analysis confirmed an increased surface Fe(II) content after reaction, supporting this synergistic mechanism. Density functional theory (DFT) calculations proved that Co sites exhibit superior adsorption capacity for PAA compared to Fe sites on three main facets. This work not only presents 0.5Co-FeOCl as a highly efficient and stable catalyst for PAA activation but also provides fundamental insights into the synergistic mechanisms in bimetallic/PAA systems for remediating refractory organic pollutants.</p>

Graphical abstract



Highlights

- A Co-doped FeOCl catalyst was synthesized to overcome the slow Fe(III)/Fe(II) cycle inherent in pure FeOCl.
- The optimized 0.5Co-FeOCl/PAA system achieved a reaction rate 5.6 times higher than the FeOCl/PAA system.
- CBZ degradation was driven by organic radicals and high-valent Fe(IV)/Co(IV) species.
- DFT calculations revealed that Co sites exhibit stronger affinity for PAA adsorption compared to Fe sites.

[Click here to view linked References](#)

1

2

3

4

5

6

7

8

9

10 a. Key Laboratory of Building Safety and Energy Efficiency, Ministry of Education,
11 College of Civil Engineering, Hunan University, Changsha 410082, China

12 b. Department of Technical Biogeochemistry, Helmholtz Centre for Environmental
13 Research – UFZ, Leipzig 04318, Germany

14

15

16

17 *Corresponding authors

18 *E-mail addresses:* zhj95@hnu.edu.cn (H. Zhang); lindeng@hnu.edu.cn (L. Deng)

19

Abstract

20
21 The widespread occurrence of carbamazepine (CBZ) in aquatic environments
22 necessitates efficient water treatment technologies. This study developed a
23 cobalt-doped iron oxychloride (Co-FeOCl) catalyst via a facile calcination method to
24 activate peracetic acid (PAA) for enhanced degradation of CBZ. The incorporation of
25 Co into the FeOCl structure dramatically boosted the catalytic performance, with
26 0.5Co-FeOCl exhibiting superior activity compared to pristine FeOCl. The
27 0.5Co-FeOCl/PAA system achieved an apparent rate constant of 0.039 min^{-1} , 19.5 and
28 5.6 times higher than that of the PAA alone (0.002 min^{-1}) and FeOCl/PAA (0.007
29 min^{-1}) systems, respectively. Mechanistic investigations revealed that the degradation
30 was primarily driven by organic radicals ($\text{CH}_3\text{C}(\text{O})\text{OO}\cdot$ and $\text{CH}_3\text{C}(\text{O})\text{O}\cdot$) and
31 high-valent metal species (Co(IV) and Fe(IV)). The Co doping established synergistic
32 Fe(II)/Fe(III)-Co(II)/Co(III) redox cycles, effectively accelerating the rate-limiting
33 Fe(III) reduction step and facilitating continuous generation of reactive species. XPS
34 analysis confirmed an increased surface Fe(II) content after reaction, supporting this
35 synergistic mechanism. Density functional theory (DFT) calculations proved that Co
36 sites exhibit superior adsorption capacity for PAA compared to Fe sites on three main
37 facets. This work not only presents 0.5Co-FeOCl as a highly efficient and stable
38 catalyst for PAA activation but also provides fundamental insights into the synergistic
39 mechanisms in bimetallic/PAA systems for remediating refractory organic pollutants.

40 **Keywords:** Co-doped FeOCl; Peracetic acid; Carbamazepine degradation; Advanced
41 oxidation processes; Synergistic mechanism

42 1. Introduction

43 Pharmaceuticals and personal care products have emerged as a pervasive class of
44 trace organic pollutants, increasingly detected in diverse environmental matrices,
45 including drinking water. Among them, carbamazepine (CBZ), a widely prescribed
46 anticonvulsant for epilepsy and trigeminal neuralgia [1], is of particular concern due
47 to its high persistence, potential for bioaccumulation, and resistance to degradation,
48 even after metabolic excretion, thereby posing significant risks to aquatic ecosystems
49 and human health [2, 3].

50 Various water treatment technologies have been explored to address this issue,
51 including membrane filtration [4], electrochemical treatment [5], adsorption [6], and
52 advanced oxidation processes (AOPs) [7]. Owing to their capacity to generate highly
53 reactive oxygen species (ROS) capable of mineralizing pollutants or converting them
54 into less toxic byproducts, AOPs represent a particularly promising solution [8].
55 Recently, peracetic acid (PAA) has gained traction as a superior alternative to
56 conventional AOP precursors like peroxymonosulfate (PMS), H₂O₂, and persulfate,
57 owing to its lower O–O bond energy, which facilitates more efficient activation [9].
58 Upon activation, PAA can produce a diverse array of reactive species [10, 11],
59 including hydroxyl radical (\bullet OH) and organic radical (R-O \bullet) [12, 13], driving the
60 development of efficient PAA-based AOPs for water decontamination [14-18].

61 PAA activation can be achieved by multiple methods, including ultraviolet
62 irradiation [19], thermal energy [20], and transition metals (e.g., Co, Cu, Mn, Fe) [21,
63 22]. Among these, transition metal-based activation is highly suited for large-scale

64 applications due to its high catalytic efficiency, broad applicability, and
65 energy-independent operation. Iron species (e.g., Fe^{2+} , Fe^{3+}) are widely employed
66 owing to their low toxicity and effectiveness. However, homogeneous Fe-catalyzed
67 systems are plagued by inherent drawbacks, including significant oxidant scavenging,
68 stringent pH dependence, difficulties in catalyst recovery, and the risk of secondary
69 pollution from residual iron ions. These limitations elevate operational costs and
70 potential environmental risks, underscoring the critical need to develop efficient,
71 eco-friendly, and reusable solid iron-based catalysts.

72 Two-dimensional layered metal oxychlorides, such as FeOCl and BiOCl , have
73 recently attracted considerable interest in catalysis due to their unique coordination
74 structures, strong visible-light absorption, and high structural tunability [23, 24].
75 FeOCl , featuring characteristic linear Cl-Fe-O and Fe-O-Fe configuration, exposes a
76 higher density of unsaturated iron sites on its surface compared to conventional iron
77 oxides (e.g., Fe_2O_3 and Fe_3O_4), thereby enhancing its catalytic potential [25, 26].
78 Despite this advantage, the practical application of FeOCl is substantially hampered
79 by the sluggish regeneration of Fe(II) from Fe(III) , which severely restricts its
80 degradation kinetics and overall efficacy [27]. Heteroatom doping has emerged as a
81 powerful strategy to overcome this kinetic limitation. Recent studies confirm that
82 bimetallic catalysts often exhibit superior performance due to synergistic inter-metal
83 effects [28]. Consequently, doping FeOCl with metals such as Zn [29], Sn [30], or Cu
84 [31] has proven effective in boosting its catalytic activity. Notably, cobalt (Co) stands
85 out among transition metals for PAA activation, given its versatile redox chemistry

86 (Co²⁺/Co³⁺), efficient electron transfer capability, and ability to modulate oxygen
87 vacancy density.

88 Inspired by these insights, we designed and synthesized a novel Co-doped FeOCl
89 (Co-FeOCl) catalyst via a facile calcination method. We hypothesize that introducing
90 Co will establish synergistic Fe(II)/Fe(III)-Co(II)/Co(III) redox cycles, thereby
91 accelerating the rate-limiting Fe(III) reduction step and enhancing the overall catalytic
92 performance. Nevertheless, research on PAA activation by Co-FeOCl remains scarce,
93 and the underlying mechanisms governing its efficacy are still elusive.

94 Therefore, this study aims to construct a Co-FeOCl/PAA system for CBZ
95 degradation. The specific objectives are to: (i) optimize the synthesis parameters of
96 Co-FeOCl; (ii) evaluate the effects of key operational conditions (e.g., initial pH,
97 catalyst and PAA dosages, and common anions) on CBZ removal; (iii) identify the
98 dominant reactive species and quantify their contributions; (iv) elucidate the
99 structure-activity relationship of the catalyst and the PAA activation mechanism; and
100 (v) propose potential CBZ degradation pathways and assess the toxicity evolution of
101 its transformation products.

102 **2. Materials and methods**

103 **2.1. Chemicals**

104 All reagents were of analytical grade and used without further purification. PAA
105 (10 wt% in water), FeCl₃·6H₂O, CoCl₂·6H₂O, NiCl₂·6H₂O, MnCl₂·4H₂O, ZnCl₂,
106 CuCl₂, H₂SO₄, NaOH, NaCl, Na₂SO₄, NaHCO₃, Na₂CO₃, and H₂O₂ were obtained
107 from Aladdin Scientific Co., Ltd. (Shanghai, China). CBZ, sulfamethoxazole (SMX),

108 sulfadiazine (SDZ), and tetracycline (TC), methanol (MeOH), tert-butanol (TBA),
109 p-benzoquinone (BQ), 2,4-hexadiene (2,4-HD), furfuryl alcohol (FFA), phenyl methyl
110 sulfoxide (PMSO), methyl phenyl sulfone (PMSO₂), 5,5-Dimethyl-1-pyrroline
111 N-oxide (DMPO), and 2,2,6,6-tetramethyl-4-piperidone (TEMP) were purchased
112 from Sigma-Aladdin Chemical Co., Ltd (Shanghai, China). Ultrapure water (18.2
113 MΩ·cm) was generated by a Millipore system (Bedford, USA).

114 **2.2. Synthesis of Co-FeOCl**

115 The x Co-FeOCl catalysts were synthesized using a one-step calcination method.
116 Specifically, varying amounts of FeCl₃·6H₂O and CoCl₂·6H₂O were dissolved in 4
117 mL of ultrapure water and sonicated for 30 min at room temperature. The mixture was
118 then dried in an oven at 70 °C for 24 h. Subsequently, the dried solid was transferred
119 to a muffle furnace, heated to 250 °C at a rate of 10 °C/min, and held at that
120 temperature for 2.5 h. After cooling naturally to room temperature, the product was
121 thoroughly washed with methanol and deionized water, dried, and ground to obtain
122 the final x Co-FeOCl material. Based on the molar ratios of CoCl₂·6H₂O to
123 FeCl₃·6H₂O (1:10, 1:5, 3:10, and 2:5), the resulting catalysts were designated as
124 0.5Co-FeOCl, 1.0Co-FeOCl, 1.5Co-FeOCl, and 2.0Co-FeOCl, respectively. For
125 comparison, Ni-, Mn-, Cu-, Zn-doped FeOCl were synthesized using the same
126 procedure.

127 **2.3. Experimental procedure**

128 Catalytic degradation experiments were conducted at ambient temperature in
129 batch mode. A 50 mL CBZ solution was prepared in a 100 mL beaker by diluting a

130 stock solution with ultrapure water. A specified dosage of Co-FeOCl catalyst was
131 added, and the mixture was stirred for 10 min to achieve adsorption–desorption
132 equilibrium. The reaction was initiated by rapidly adding the PAA solution.
133 Subsequently, 0.5 mL aliquots were collected at prescribed time intervals (0, 10, 20,
134 30, 40, 50, and 60 min), immediately filtered through 0.22 μm membranes, and
135 quenched with an equal volume of methanol for analysis. If necessary, the initial pH
136 of the solution was adjusted to a pre-determined value using 0.1 M H_2SO_4 or 0.1 M
137 NaOH. The solution pH was measured by a pH meter (PHS-3C, INESA Scientific
138 Instrument, China). The relative standard deviation was consistently below 5%.
139 Quenching experiments were carried out by adding MeOH, BQ, TBA, FFA, Mn^{2+} ,
140 PMSO, and 2,4-HD as scavengers. All degradation experiments were performed in
141 triplicate.

142 **2.4. Catalysts characterization and analytical methods**

143 Scanning electron microscopy (SEM, ZEISS Sigma 300) was used to examine
144 the surface morphology. High-resolution transmission electron microscopy (HRTEM,
145 Thermo Fisher Talos F200X G2) and energy-dispersive X-ray spectroscopy (EDX,
146 JEM-2100F) were employed to analyze microstructure and elemental distribution.
147 X-ray diffraction (XRD, D8 Advance, Bruker) with Ni-filtered $\text{Cu K}\alpha$ radiation (scan
148 rate: $0.02^\circ/\text{s}$ in 2θ) was performed to determine crystallinity and phase composition.
149 X-ray photoelectron spectroscopy (XPS, Thermo Scientific K-Alpha) was conducted
150 to analyze surface elemental composition and chemical states. Fourier transform
151 infrared spectroscopy (FTIR, Thermo Fisher Scientific Nicolet iS20) was used to

152 identify functional groups. Element content was analyzed by inductively coupled
153 plasma mass spectrometer (ICP-OES, Agilent 7800MS). The electron spin resonance
154 (ESR) spectra were recorded by an ESR spectrometer (Bruker EMXnano, Germany).

155 Analytical details are provided in [Text S1 \(Supplementary Material\)](#). The
156 concentration of CBZ was measured by high-performance liquid chromatography
157 (HPLC, Waters 2695) equipped with diode array detector (PDA waters 2998) and
158 fluorescence detector (Waters 2475). An Waters symmetry C18 column
159 (4.6 mm × 150 mm, 5 μm particle size) was used. The HPLC analysis parameters for
160 CBZ, SMX, SDZ, TC, PMSO, PMSO₂ are listed in [Table S1](#).

161 **3. Results and discussion**

162 **3.1. Optimization of synthesis parameters for *x*-Co-FeOCl**

163 The catalytic activities of various transition metal-doped FeOCl catalysts
164 (M-FeOCl, M = Co, Ni, Mn, Cu, Zn) were evaluated for PAA activation. As shown in
165 [Figure 1a](#), the Co-FeOCl/PAA system exhibited superior performance, achieving over
166 90% degradation of CBZ within 60 min using 0.1 g/L of Co-FeOCl and 0.6 mM of
167 PAA. In contrast, Ni-, Mn-, Cu-, and Zn-doped FeOCl catalysts showed moderate to
168 low activities. The remarkable efficiency of Co-FeOCl is attributed to the strong
169 redox capability of cobalt and its synergistic effect with iron, promoting efficient PAA
170 activation. The apparent first-order rate constants (k_{obs}) followed the order: Co-FeOCl
171 (0.039 min^{-1}) > Ni-FeOCl (0.027 min^{-1}) > Mn-FeOCl (0.011 min^{-1}) > Cu-FeOCl
172 (0.004 min^{-1}) > Zn-FeOCl (0.003 min^{-1}) ([Figure S1](#)).

173 Control experiments confirmed the necessity of both the catalyst and the oxidant.
174 As depicted in [Figure 1b](#), negligible CBZ removal was observed with PAA alone or
175 0.5Co-FeOCl alone. The FeOCl/PAA system achieved only 31.5% removal after 60
176 min. In sharp contrast, the 0.5Co-FeOCl/PAA system removed over 90% of CBZ
177 within the same timeframe, highlighting the synergy between Co doping and PAA
178 activation. The k_{obs} value for the 0.5Co-FeOCl/PAA system (0.039 min^{-1}) was 19.5
179 and 5.6 times higher than those of PAA alone (0.002 min^{-1}) and FeOCl/PAA (0.007
180 min^{-1}) ([Figure S2](#)), respectively. These results clearly demonstrate that Co doping
181 significantly enhances the catalytic activity of FeOCl and that PAA activation is the
182 primary pathway for CBZ degradation.

183 The influence of Co doping content was further investigated. As shown in [Figure](#)
184 [1c](#), the catalytic activity of $x\text{Co-FeOCl}$ was highly dependent on the doping ratio, with
185 an optimal concentration yielding the highest degradation efficiency. Both lower and
186 higher doping levels reduced performance, indicating the importance of balancing the
187 number of active sites and electron transfer efficiency. Catalyst stability was assessed
188 by measuring metal leaching (Fe and Co). [Figure 1d](#) shows that the leached Fe
189 concentration remained consistently low ($0.5\text{--}0.6 \text{ mg/L}$) across all samples, while Co
190 leaching increased significantly with higher doping levels. Considering both activity
191 and environmental safety, 0.5Co-FeOCl was selected for further study.

192 **3.2. Catalysts characterizations**

193 The surface morphology of the as-synthesized catalysts was examined by SEM
194 and TEM. As shown in [Figure 2a](#) and [b](#), both FeOCl and 0.5Co-FeOCl display a flat,

195 smooth surface composed of well-defined solid flakes (4–18 μm in length) stacked in
196 a layered architecture (Figure 2c), which is characteristic of the FeOCl structure. EDS
197 elemental mapping (Figure 2d) confirms the homogeneous distribution of Co, Fe, O,
198 and Cl throughout the 0.5Co-FeOCl sample. XRD analysis (Figure 2e) shows that the
199 pristine FeOCl exhibits distinct diffraction peaks at $2\theta = 24.3^\circ, 34.0^\circ, 36.0^\circ, 41.2^\circ,$
200 $49.9^\circ, 54.6^\circ, 62.6^\circ,$ and 64.4° , corresponding to the (110), (021), (111), (130), (131),
201 (002), (221), and (150) crystal planes, respectively. These peaks match well with the
202 standard reference pattern for β -FeOCl (JCPDS No. 24-1005), confirming the
203 successful formation of a crystalline FeOCl phase. Importantly, the introduction of Co
204 did not induce significant changes, and 0.5Co-FeOCl retained the fundamental FeOCl
205 framework, with sharp and intense diffraction peaks indicating high crystallinity.
206 FTIR spectra was collected to compare the functional groups present in pure FeOCl
207 and 0.5Co-FeOCl (Figure 2f). Both samples exhibit a broad absorption band around
208 $3418.0\text{--}3421.8\text{ cm}^{-1}$, potentially indicating the presence of very strongly
209 hydrogen-bonded or distinct metal–hydroxyl (M–OH) environments. As for the
210 0.5Co-FeOCl, the band at 1606.4 cm^{-1} can correspond to H–O–H bending vibrations
211 of adsorbed water. The band at 1371.3 cm^{-1} is related to deformation vibrations of
212 metal–bonded hydroxyl groups (M–OH). The peak at 804.7 cm^{-1} likely arises from
213 metal–oxygen stretching vibrations. It could be associated with the formation of Co–O
214 bonds or modified Fe–O bonds within the lattice. The absorption bands below 750
215 cm^{-1} are characteristic of metal–oxygen (M–O) stretching vibrations in metal oxide
216 lattices. In the XPS Cl 2p spectra (Figure 2g), 0.5Co-FeOCl exhibits peaks at binding

217 energies of 198.9 eV (Cl 2p_{3/2}) and 200.5 eV (Cl 2p_{1/2}), corresponding to the covalent
218 Fe–Cl bonds. The Fe 2p spectra (Figure 2h) shows coexisting Fe(II) (711.2 eV and
219 723.9 eV) and Fe(III) (726.1 eV and 712.4 eV).

220 In conclusion, SEM, TEM, XRD, FTIR, and XPS analyses confirm the
221 successful synthesis of 0.5Co-FeOCl catalyst while perfectly preserving the parent
222 FeOCl crystal structure.

223 3.3. Influence of key operational parameters on CBZ removal

224 The efficacy of the 0.5Co-FeOCl/PAA system was evaluated under various
225 operational parameters. As shown in Figure 3a, CBZ degradation exhibited a positive
226 correlation with catalyst dosage (0.04 to 0.20 g/L). The highest dosage (0.20 g/L)
227 achieved near-complete CBZ removal within 30 min, indicating a surface-reaction
228 limited process under these conditions. Similarly, increasing PAA concentration from
229 0.3 mM to 1.5 mM enhanced CBZ removal from 61.2% to 100% (Figure 3b),
230 underscoring the critical role of oxidant availability.

231 The initial solution pH also exerted a profound influence (Figure 3c). The
232 removal of CBZ by the 0.5Co-FeOCl/PAA system was strongly suppressed at pH 3.0,
233 peaked at over 90% removal at neutral pH (7.0), and declined to 53.4% at pH 9.0.
234 This pH-dependent behavior is attributed to catalyst surface charge and PAA
235 speciation. In acidic media, protonated PAA experiences electrostatic repulsion with
236 positively charged active sites (Co²⁺, Fe²⁺), hindering electron transfer and the
237 formation of reactive species [32]. The decreased performance under alkaline

238 conditions is primarily related to PAA self-decomposition and inactive iron/cobalt
239 hydroxide precipitates formation [32-34].

240 The influence of common coexisting inorganic anions (Cl^- , SO_4^{2-} , HCO_3^- , CO_3^{2-})
241 on CBZ degradation is presented in Figure 3d. A significant inhibitory effect was
242 observed in the presence of HCO_3^- and CO_3^{2-} , which can be ascribed to multiple
243 mechanisms: (i) their hydrolysis increases the solution pH, creating unfavorable
244 alkaline conditions; (ii) they act as scavengers of reactive peroxygen species [35, 36];
245 and they may form surface complexes that passivate active sites [33]. In contrast, Cl^-
246 and SO_4^{2-} exhibited only minor effects, with CBZ removal remaining comparable to
247 the anion-free control. This marked contrast highlights the critical role of carbonate
248 species in determining the system's applicability in complex water matrices. To gauge
249 its practical potential, the system underwent evaluation using SMX, SDZ, and TC,
250 common antibiotic pollutants exhibiting diverse molecular structures. As shown in
251 Figure S3, over 90% removal of each compound was achieved within 60 min,
252 demonstrating the strong effectiveness and broad applicability of the
253 0.5Co-FeOCl/PAA system for degrading diverse organic pollutants in water treatment.
254 XRD patterns of fresh and used 0.5Co-FeOCl showed no detectable structural
255 changes (Figure S4), attesting to the catalyst's stability.

256 **3.4. Mechanisms for CBZ degradation in the 0.5Co-FeOCl/PAA system**

257 *3.4.1 Identification of reactive species*

258 PAA-based AOPs can generate a diverse range of reactive species capable of
259 degrading organic pollutants, including $\bullet\text{OH}$, $\text{O}_2\bullet^-$, $^1\text{O}_2$, and organic radicals such as

260 acetylperoxy ($\text{CH}_3\text{C}(\text{O})\text{O}\cdot$), peracetyl ($\text{CH}_3\text{C}(\text{O})\text{OO}\cdot$), methylperoxy ($\text{CH}_3\text{OO}\cdot$), and
261 methyl ($\text{CH}_3\cdot$) radicals [37]. To identify the dominant reactive species, quenching
262 experiments were performed using several scavengers: MeOH for $\cdot\text{OH}$ and organic
263 radicals; TBA as a selective $\cdot\text{OH}$ quencher ($k = 3.8\text{--}7.6 \times 10^8 \text{ M}^{-1} \text{ s}^{-1}$); 2,4-HD and
264 Mn^{2+} for $\text{CH}_3\text{C}(\text{O})\text{O}\cdot$ and $\text{CH}_3\text{C}(\text{O})\text{OO}\cdot$, respectively; BQ for $\text{O}_2^{\cdot-}$ ($k = 2.9 \times 10^9 \text{ M}^{-1} \text{ s}^{-1}$);
265 FFA for both $\cdot\text{OH}$ ($k = 1.5 \times 10^{10} \text{ M}^{-1} \text{ s}^{-1}$) and $^1\text{O}_2$ ($k = 1.2 \times 10^8 \text{ M}^{-1} \text{ s}^{-1}$); and PMSO
266 for high-valent metal-oxo species. As shown in Figure 4a, the addition of MeOH (50
267 mM) caused the most striking inhibition (5.6% CBZ removal). TBA (50 mM) reduced
268 the removal to 71.3%, implicating the contribution of both $\cdot\text{OH}$ and organic radicals,
269 with the latter exerting a more dominant influence. BQ and FFA slashed efficiency to
270 44.6% and 50.3%, respectively, confirming the participation of $\text{O}_2^{\cdot-}$ and $^1\text{O}_2$. 2,4-HD
271 and Mn^{2+} markedly reduced the degradation to 22.3% and 19.1%, highlighting the
272 crucial contribution of $\text{CH}_3\text{C}(\text{O})\text{O}\cdot$ and $\text{CH}_3\text{C}(\text{O})\text{OO}\cdot$. Also, PMSO profoundly
273 inhibited the degradation (15.5% removal), underscoring the role of high-valent
274 metal-oxo species.

275 Electron paramagnetic resonance (EPR) spectroscopy can provide direct
276 evidence of radical generation. As shown in Figure 4b-c, characteristic signals of
277 DMPO- $\text{ROO}\cdot$, DMPO- $\cdot\text{OH}$, and TEMP- $^1\text{O}_2$ adducts were detected, confirming the
278 formation of $\text{ROO}\cdot$, $\cdot\text{OH}$, and $^1\text{O}_2$ [38, 39]. To probe high-valent metal species, we
279 employed PMSO, a substrate selectively oxidized to PMSO_2 by high-valent metal-oxo
280 species [32]. As shown in Figure 4d, 37.7% of PMSO was consumed over 60 min,
281 with 44.8% of the consumed amount stoichiometrically converted to PMSO_2 (1.69

282 μM), providing compelling evidence for the involvement of high-valent Fe(IV)/Co(IV)
283 species.

284 In summary, CBZ degradation in the 0.5Co-FeOCl/PAA system was driven by
285 multiple reactive species, with organic radicals ($\text{CH}_3\text{C}(\text{O})\text{OO}\cdot/\text{CH}_3\text{C}(\text{O})\text{O}\cdot$) and
286 high-valent Fe(IV)/Co(IV) playing major roles.

287 *3.4.2 XPS analysis of 0.5Co-FeOCl before and after reaction*

288 XPS analysis probed the evolution of chemical states in 0.5Co-FeOCl during the
289 catalytic reaction (Figure 5). The Fe–Cl peak in the Cl 2p spectra remained observable
290 in the used catalyst, confirming structural stability (Figure 5a) [40]. In the O 1s
291 spectra (Figure 5b), three distinct components were identified: lattice oxygen (O_L ,
292 530.5 eV), surface hydroxyl groups (O_A , 531.9 eV), and physically adsorbed H_2O (O_H ,
293 532.3 eV). After reaction, the O_L content surged from 14.2% to 39.4%, while O_A
294 plummeted from 59.9% to 9.9%, and O_H increased from 25.9% to 50.7%. This
295 transformation indicates direct involvement of surface hydroxyl groups in the
296 catalytic process. Deconvolution of the Fe 2p_{3/2} region (Figure 5c) revealed Fe(II)
297 (711.1 eV) and Fe(III) (712.6 eV) [40, 41], with relative contents of 36.19% and
298 63.81%, respectively [42]. After catalytic, the peaks shifted to lower binding energies
299 (711.3 eV and 724.9 eV, respectively), and the Fe(II) content increased to 70.71% in
300 the Fe 2p_{3/2} region, strongly supporting the involvement of iron redox cycling [43].
301 The Co 2p spectrum (Figure 5d) exhibited an atypical line shape, attributable to low
302 cobalt loading and an elevated background signal [44, 45].

303 *3.4.3 DFT calculations of PAA adsorption on various facets*

304 To further elucidate the role of doped Co atoms, DFT calculations were
305 performed to investigate the adsorption of PAA on the dominant facets of FeOCl and
306 0.5Co-FeOCl (see [Text S2](#) for details). Based on XRD analysis, the (111), (110), and
307 (021) facets were identified as the predominant facets for both materials. The
308 optimized adsorption configurations of PAA on these facets of FeOCl and
309 0.5Co-FeOCl are shown in [Figure 5e](#) and [f](#), respectively. In all cases, the Fe and Co
310 metal sites act as the primary adsorption centers for PAA. The calculated adsorption
311 energies (E_{ad}) of PAA on the (111), (110), and (021) facets of FeOCl are -2.93 , -8.21 ,
312 and -2.26 eV, respectively. For 0.5Co-FeOCl, the corresponding E_{ad} values are -3.78 ,
313 -8.66 , and -3.06 eV. The (110) facet exhibits notably stronger adsorption, which can
314 be attributed to its higher density of exposed metal sites. Importantly, across all three
315 facets, Co sites show higher affinity for PAA adsorption compared to Fe sites,
316 highlighting the crucial role of Co in promoting PAA activation. Differential charge
317 density analysis further reveals that the amount of charge transfer follows the same
318 trend as the adsorption energy. The (110) facet demonstrates the largest charge
319 transfer, with values of $0.70 e^-$ for FeOCl and $0.72 e^-$ for 0.5Co-FeOCl. Moreover,
320 charge transfer from Co sites to PAA consistently exceeds that from Fe sites. These
321 results strongly corroborate the significant contribution of Co doping to PAA
322 activation at the atomic level.

323 *3.4.4 Proposed degradation pathways of CBZ*

324 The degradation pathway of CBZ in the 0.5Co-FeOCl/PAA system was
325 investigated by identifying thirteen intermediates via liquid chromatography–mass

326 spectrometry (LC–MS) (Table S2). As shown in Figure 6, three primary degradation
327 routes are proposed, initiated by reactive species (primarily organic radicals, Fe(IV),
328 and Co(VI)). In Pathway I, the central C=C double bond of CBZ undergoes
329 hydroxylation, forming P1 (m/z 253). This intermediate is further oxidized, leading to
330 dihydroxylated (e.g., P2, m/z 271) or ketone derivatives (e.g., P3, m/z 269) via
331 subsequent attacks on the azepine ring. Pathway II involves more extensive structural
332 destruction, culminating in azepine ring opening. CBZ or its hydroxylated derivatives
333 (e.g., P1) undergo ring rearrangement and contraction, often accompanied by
334 decarboxylation ($-\text{CO}_2$) or loss of the $-\text{CONH}_2$ group, to yield the six-membered ring
335 intermediate P6 (m/z 210). Subsequent oxidative cleavage of this contracted ring
336 generates smaller fragments such as P7 (m/z 180) and P8 (m/z 251). Ultimately, the
337 cleavage products are subjected to further radical attacks, breaking C–N and C–C
338 bonds and yielding a series of low-molecular-weight carboxylic acids. This is
339 evidenced by the detection of P9 (m/z 198) and P4 (m/z 224) from partial cleavage;
340 P10 (m/z 139) and P11 (m/z 123) from further fragmentation; and finally, P12 (m/z
341 111) and P13 (m/z 99), which represent the ultimate products before mineralization
342 (e.g., succinic, oxaloacetic, or oxalic acid derivatives). These small acids can
343 ultimately be mineralized to CO_2 and H_2O [46-48].

344 *3.4.5 Proposed mechanisms for CBZ degradation in the 0.5Co-FeOCl/PAA system*

345 A proposed catalytic mechanism for CBZ degradation in the 0.5Co-FeOCl/PAA
346 system is illustrated in Figure 7. The process is driven by the redox cycling of
347 Fe(II)/Fe(III) and Co(II)/Co(III), which facilitates the generation of radicals species

348 and high-valent Fe(IV) and Co(IV) species. Initially, surface Fe(II) and Co(II) sites on
349 the catalyst coordinate with adsorbed PAA, forming Fe(II)-PAA and Co(II)-PAA
350 complexes. These complexes undergo intramolecular electron transfer, decomposing
351 to produce Fe(III) and Co(III) alongside the $\text{CH}_3\text{C}(\text{O})\text{O}\cdot$ radicals. The resulting Fe(III)
352 and Co(III) can subsequently complex with another PAA molecule (forming Fe(III)-
353 PAA and Co(III)-PAA) and be reduced back to Fe(II) and Co(II), thereby generating
354 $\text{CH}_3\text{C}(\text{O})\text{OO}\cdot$. Alternatively, the Fe(II)-PAA and Co(II)-PAA complexes may proceed
355 via a two-electron transfer pathway, directly yielding highly oxidizing Fe(IV) and
356 Co(IV) species.

357 **4. Conclusions**

358 In this study, a Co-doped FeOCl catalyst was successfully synthesized and
359 employed to activate PAA for the efficient degradation of CBZ. Co doping
360 significantly enhanced the catalytic activity of FeOCl. The optimized
361 0.5Co-FeOCl/PAA system achieved excellent CBZ removal, substantially
362 outperforming pure FeOCl and other transition-metal-doped FeOCl catalysts,
363 highlighting the unique synergy between Co and Fe. Notably, 0.5Co-FeOCl exhibited
364 a favorable balance between high catalytic activity and low metal leaching, suggesting
365 its potential for practical application. Mechanistic investigations revealed that the
366 system operated through a unique combination of organic radicals
367 ($\text{CH}_3\text{C}(\text{O})\text{OO}\cdot/\text{CH}_3\text{C}(\text{O})\text{O}\cdot$) and high-valent Fe(IV)/Co(IV) species. The introduction
368 of Co efficiently promoted the regeneration of Fe(II) from Fe(III), establishing a
369 synergistic catalytic cycle that enhanced PAA activation. DFT calculations further

370 indicated that Co sites possess superior PAA adsorption capacity over Fe sites on three
371 dominant (111), (110) and (021) facets. Based on intermediates analysis, possible
372 degradation pathways involving hydroxylation, ring contraction, and bond cleavage
373 were proposed. This work not only presents 0.5Co-FeOCl as a highly effective
374 catalyst for PAA-based AOPs, but also offers fundamental insight into the synergistic
375 mechanisms in bimetallic/PAA systems, thereby supporting their future application
376 for eliminating persistent organic pollutants from water.

377

378 **Acknowledgments**

379 This work was financially supported by National Natural Science Foundation of
380 China (52270004).

381 **References**

- 382 [1] S. Remy, S. Gabriel, B.W. Urban, D. Dietrich, T.N. Lehmann, C.E. Elger, U. Heinemann, H. Beck,
383 A novel mechanism underlying drug resistance in chronic epilepsy, *Annals of Neurology* 53(4) (2003)
384 469–479. <https://doi.org/https://doi.org/10.1002/ana.10473>.
- 385 [2] L. Bo, K. He, N. Tan, B. Gao, Q. Feng, J. Liu, L. Wang, Photocatalytic oxidation of trace
386 carbamazepine in aqueous solution by visible-light-driven ZnIn₂S₄: Performance and mechanism,
387 *Journal of Environmental Management* 190 (2017) 259–265.
388 <https://doi.org/10.1016/j.jenvman.2016.12.050>.
- 389 [3] R. Moreno-González, S. Rodríguez-Mozaz, M. Gros, E. Pérez-Cánovas, D. Barceló, V.M. León,
390 Input of pharmaceuticals through coastal surface watercourses into a Mediterranean lagoon (Mar
391 Menor, SE Spain): Sources and seasonal variations, *Science of The Total Environment* 490 (2014) 59–
392 72. <https://doi.org/10.1016/j.scitotenv.2014.04.097>.
- 393 [4] Z. Liao, M.N. Nguyen, G. Wan, J. Xie, L. Ni, J. Qi, J. Li, A.I. Schäfer, Low pressure operated
394 ultrafiltration membrane with integration of hollow mesoporous carbon nanospheres for effective
395 removal of micropollutants, *Journal of Hazardous Materials* 397 (2020).
396 <https://doi.org/10.1016/j.jhazmat.2020.122779>.
- 397 [5] C. Dai, D. Chen, J. Wu, J. Liu, S. Shi, J. Zhang, Y. Feng, Construction of a novel integrated
398 electrochemical oxidation-coagulation system for simultaneous removal of suspended solids and
399 antibiotics, *Chemical Engineering Journal* 447 (2022). <https://doi.org/10.1016/j.cej.2022.137505>.
- 400 [6] P. Liu, Q. Wang, C. Zheng, C. He, Sorption of Sulfadiazine, Norfloxacin, Metronidazole, and
401 Tetracycline by Granular Activated Carbon: Kinetics, Mechanisms, and Isotherms, *Water, Air, & Soil*
402 *Pollution* 228(4) (2017). <https://doi.org/10.1007/s11270-017-3320-x>.
- 403 [7] Y. Zhang, Y.-G. Zhao, F. Maqbool, Y. Hu, Removal of antibiotics pollutants in wastewater by
404 UV-based advanced oxidation processes: Influence of water matrix components, processes
405 optimization and application: A review, *Journal of Water Process Engineering* 45 (2022).
406 <https://doi.org/10.1016/j.jwpe.2021.102496>.
- 407 [8] A.V. Karim, A. Hassani, P. Eghbali, P.V. Nidheesh, Nanostructured modified layered double
408 hydroxides (LDHs)-based catalysts: A review on synthesis, characterization, and applications in water
409 remediation by advanced oxidation processes, *Current Opinion in Solid State and Materials Science*
410 26(1) (2022). <https://doi.org/10.1016/j.cossms.2021.100965>.
- 411 [9] T. Luukkonen, S. Pehkonen, Peracids in water treatment: A critical review, *Critical Reviews in*
412 *Environmental Science and Technology* 47(1) (2017) 1–39.
413 <https://doi.org/10.1080/10643389.2016.1272343>.
- 414 [10] F. Chen, L. Liu, J. Wu, X. Rui, J. Chen, Y. Yu, Single-Atom Iron Anchored Tubular g-C₃N₄
415 Catalysts for Ultrafast Fenton-Like Reaction: Roles of High-Valency Iron-Oxo Species and Organic
416 Radicals, *Advanced Materials* 34(31) (2022). <https://doi.org/10.1002/adma.202202891>.
- 417 [11] T. Yang, L. An, G. Zeng, M. Jiang, J. Li, C. Liu, J. Jia, J. Ma, Efficient removal of p-arsanilic acid
418 and arsenite by Fe(II)/peracetic acid (Fe(II)/PAA) and PAA processes, *Water Research* 241 (2023).
419 <https://doi.org/10.1016/j.watres.2023.120091>.
- 420 [12] J. Hollman, J. Dominic, G. Achari, Degradation of pharmaceutical mixtures in aqueous solutions
421 using UV/peracetic acid process: Kinetics, degradation pathways and comparison with UV/H₂O₂,
422 *Chemosphere* 248 (2020). <https://doi.org/10.1016/j.chemosphere.2020.125911>.
- 423 [13] W. Sun, K. Pang, F. Ye, M. Pu, C. Zhou, H. Huang, Q. Zhang, J. Niu, Carbonization of camphor
424 sulfonic acid and melamine to N,S-co-doped carbon for sulfamethoxazole degradation via persulfate

425 activation: Nonradical dominant pathway, *Separation and Purification Technology* 279 (2021).
426 <https://doi.org/10.1016/j.seppur.2021.119723>.

427 [14] C. Zhang, P. Brown, Z. Hu, Thermodynamic properties of an emerging chemical disinfectant,
428 peracetic acid, *Science of the Total Environment* 621 (2018) 948–959.
429 <https://doi.org/10.1016/j.scitotenv.2017.10.195>.

430 [15] J. Lee, U. von Gunten, J. Kim, Persulfate-Based Advanced Oxidation: Critical Assessment of
431 Opportunities and Roadblocks, *Environmental Science & Technology* 54(6) (2020) 3064–3081.
432 <https://doi.org/10.1021/acs.est.9b07082>.

433 [16] X. Ao, J. Eloranta, C. Huang, D. Santoro, W. Sun, Z. Lu, C. Li, Peracetic acid-based advanced
434 oxidation processes for decontamination and disinfection of water: A review, *Water Research* 188
435 (2021). <https://doi.org/10.1016/j.watres.2020.116479>.

436 [17] D. Miklos, C. Remy, M. Jekel, K. Linden, J. Drewes, U. Hübner, Evaluation of advanced
437 oxidation processes for water and wastewater treatment - A critical review, *Water Research* 139 (2018)
438 118–131. <https://doi.org/10.1016/j.watres.2018.03.042>.

439 [18] M. Priyadarshini, I. Das, M. Ghangrekar, L. Blaney, Advanced oxidation processes: Performance,
440 advantages, and scale-up of emerging technologies, *Journal of Environmental Management* 316 (2022).
441 <https://doi.org/10.1016/j.jenvman.2022.115295>.

442 [19] W. Wu, D. Tian, T. Liu, J. Chen, T. Huang, X. Zhou, Y. Zhang, Degradation of organic compounds
443 by peracetic acid activated with Co₃O₄: A novel advanced oxidation process and organic radical
444 contribution, *Chemical Engineering Journal* 394 (2020). <https://doi.org/10.1016/j.cej.2020.124938>.

445 [20] J. Wang, Y. Wan, J. Ding, Z. Wang, J. Ma, P. Xie, M. Wiesner, Thermal Activation of Peracetic
446 Acid in Aquatic Solution: The Mechanism and Application to Degrade Sulfamethoxazole,
447 *Environmental Science & Technology* 54(22) (2020) 14635–14645.
448 <https://doi.org/10.1021/acs.est.0c02061>.

449 [21] J. Dong, W. Xu, S. Liu, Y. Gong, T. Yang, L. Du, Q. Chen, X. Tan, Y. Liu, Lignin-derived biochar
450 to support CoFe₂O₄: Effective activation of peracetic acid for sulfamethoxazole degradation, *Chemical*
451 *Engineering Journal* 430 (2022). <https://doi.org/10.1016/j.cej.2021.132868>.

452 [22] J. Kim, P. Du, W. Liu, C. Luo, H. Zhao, C. Huang, Cobalt/Peracetic Acid: Advanced Oxidation of
453 Aromatic Organic Compounds by Acetylperoxyl Radicals, *Environmental Science & Technology* 54(8)
454 (2020) 5268–5278. <https://doi.org/10.1021/acs.est.0c00356>.

455 [23] J. Wang, Y. Li, Q. Jiang, S. Tong, Study on why FeOCl has high Fenton activity in wide range of
456 initial pH and its corresponding stability, *Process Safety and Environmental Protection* 172 (2023)
457 652–658. <https://doi.org/10.1016/j.psep.2023.02.050>.

458 [24] C. Tan, Q. Xu, T. Sheng, X. Cui, Z. Wu, H. Gao, H. Li, Reactive oxygen species generation in
459 FeOCl nanosheets activated peroxydisulfate system: Radicals and non-radical pathways, *Journal of*
460 *Hazardous Materials* 398 (2020). <https://doi.org/10.1016/j.jhazmat.2020.123084>.

461 [25] Y. Cao, K. Cui, Y. Chen, M. Cui, G. Li, D. Li, X. Yang, Efficient degradation of tetracycline by
462 H₂O₂ catalyzed by FeOCl: A wide range of pH values from 3 to 7, *Solid State Sciences* 113 (2021).
463 <https://doi.org/10.1016/j.solidstatesciences.2021.106548>.

464 [26] V. Nguyen, M. Mousavi, J. Ghasemi, Q. Le, S. Delbari, M. Asl, M. Shokouhimehr, M.
465 Mohammadi, Y. Azizian-Kalenderagh, A. Namini, In situ preparation of g-C₃N₄ nanosheet/FeOCl:
466 Achievement and promoted photocatalytic nitrogen fixation activity (Publication with Expression of
467 Concern. See vol. 616, 2022), *Journal of Colloid and Interface Science* 587 (2021) 538–549.
468 <https://doi.org/10.1016/j.jcis.2020.11.011>.

469 [27] D. Sun, B. Shen, S. Yang, X. Cheng, Q. Zhong, S. Abbas, Y. Dai, Y. Liu, C. Xu, C. Qi, H. He, S. Li,
470 Nitrogen-doped CNTs enhance heterogeneous Fenton reaction for IOH removal by FeOCl: Role of
471 NCNTs and mechanism, Separation and Purification Technology 326 (2023).
472 <https://doi.org/10.1016/j.seppur.2023.124763>.

473 [28] M. Danish, X. Gu, S. Lu, A. Ahmad, M. Naqvi, U. Farooq, X. Zhang, X. Fu, Z. Miao, Y. Xue,
474 Efficient transformation of trichloroethylene activated through sodium percarbonate using
475 heterogeneous zeolite supported nano zero valent iron-copper bimetallic composite, Chemical
476 Engineering Journal 308 (2017) 396–407. <https://doi.org/10.1016/j.cej.2016.09.051>.

477 [29] C. Lu, C. Jiao, Z. Wei, Zn-doped FeOCl nanosheets enable accelerated tetracycline degradation
478 via simulated sunlight-responsive photo-Fenton catalysis, Materials Science in Semiconductor
479 Processing 194 (2025). <https://doi.org/10.1016/j.mssp.2025.109542>.

480 [30] Q. Yu, M. Ding, Z. Wei, Z. Li, J. Zhao, H. Zhang, Photoelectrochemical studies of Sn doped
481 FeOCl and photo-Fenton degradation of tetracycline, Journal of Solid State Chemistry 337 (2024).
482 <https://doi.org/10.1016/j.jssc.2024.124816>.

483 [31] A. Li, Y. Wu, J. Zhou, X. Wang, Activation of peroxymonosulfate by Cu-doped iron oxychloride
484 biochar for the degradation of tetracycline and disinfection of its resistant bacteria, Journal of Water
485 Process Engineering 68 (2024). <https://doi.org/10.1016/j.jwpe.2024.106318>.

486 [32] Z. Wang, J. Wang, B. Xiong, F. Bai, S. Wang, Y. Wan, L. Zhang, P. Xie, M. Wiesner, Application
487 of Cobalt/Peracetic Acid to Degrade Sulfamethoxazole at Neutral Condition: Efficiency and
488 Mechanisms, Environmental Science & Technology 54(1) (2020) 464–475.
489 <https://doi.org/10.1021/acs.est.9b04528>.

490 [33] Y. Ren, L. Lin, J. Ma, J. Yang, J. Feng, Z. Fan, Sulfate radicals induced from peroxymonosulfate
491 by magnetic ferrosphalite MFe₂O₄ (M = Co, Cu, Mn, and Zn) as heterogeneous catalysts in the water,
492 Applied Catalysis B: Environmental 165 (2015) 572–578. <https://doi.org/10.1016/j.apcatb.2014.10.051>.

493 [34] Z. Yuan, Y. Ni, A.R.P.V. Heiningen, Kinetics of the peracetic acid decomposition: Part II: pH effect
494 and alkaline hydrolysis, The Canadian Journal of Chemical Engineering (1997).

495 [35] J. Tomasi, M. Persico, Molecular Interactions in Solution: An Overview of Methods Based on
496 Continuous Distributions of the Solvent, Cheminform 26(8) (1995).

497 [36] Y. Ji, Y. Fan, K. Liu, D. Kong, J. Lu, Thermo activated persulfate oxidation of antibiotic
498 sulfamethoxazole and structurally related compounds, Water Research 87 (2015) 1–9.
499 <https://doi.org/10.1016/j.watres.2015.09.005>.

500 [37] D. Barton, V. Le Gloahec, J. Smith, Study of a new reaction: Trapping of peroxy radicals by
501 TEMPO, Tetrahedron Letters 39(41) (1998) 7483–7486.
502 [https://doi.org/10.1016/S0040-4039\(98\)01628-1](https://doi.org/10.1016/S0040-4039(98)01628-1).

503 [38] D.F. Evans, M.W. Upton, Studies on singlet oxygen in aqueous solution. Part 3. The
504 decomposition of peroxy-acids, Journal of the Chemical Society Dalton Transactions (6) (1985) 1151.

505 [39] S. Li, Y. Yang, H. Zheng, Y. Zheng, C.-S. He, B. Lai, J. Ma, J. Nan, Introduction of
506 oxygen vacancy to manganese ferrite by Co substitution for enhanced peracetic acid activation and
507 1O₂ dominated tetracycline hydrochloride degradation under microwave irradiation, Water Research
508 225 (2022). <https://doi.org/10.1016/j.watres.2022.119176>.

509 [40] M. Sun, I. Zucker, D. Davenport, X. Zhou, J. Qu, M. Elimelech, Reactive, Self-Cleaning
510 Ultrafiltration Membrane Functionalized with Iron Oxychloride Nanocatalysts, Environmental Science
511 & Technology 52(15) (2018) 8674–8683. <https://doi.org/10.1021/acs.est.8b01916>.

512 [41] C. Tan, X. Jian, Y. Dong, X. Lu, X. Liu, H. Xiang, X. Cui, J. Deng, H. Gao, Activation of

513 peroxymonosulfate by a novel EGCE@Fe₃O₄ nanocomposite: Free radical reactions and implication
514 for the degradation of sulfadiazine, *Chemical Engineering Journal* 359 (2019) 594–603.
515 <https://doi.org/10.1016/j.cej.2018.11.178>.

516 [42] Y. Yao, Y. Cai, F. Lu, F. Wei, X. Wang, S. Wang, Magnetic recoverable MnFe₂O₄ and
517 MnFe₂O₄-graphene hybrid as heterogeneous catalysts of peroxymonosulfate activation for efficient
518 degradation of aqueous organic pollutants, *Journal of Hazardous Materials* 270(apr.15) (2014) 61–70.

519 [43] M. Chen, H. Xu, Q. Wang, D. Li, D. Xia, Activation mechanism of sodium percarbonate by FeOCl
520 under visible-light-enhanced catalytic oxidation, *Chemical Physics Letters* 706 (2018) 415–420.
521 <https://doi.org/10.1016/j.cplett.2018.06.004>.

522 [44] J. Liu, R. Meng, J. Li, P. Jian, L. Wang, R. Jian, Achieving high-performance for catalytic
523 epoxidation of styrene with uniform magnetically separable CoFe₂O₄ nanoparticles, *Applied Catalysis*
524 *B-Environmental* 254 (2019) 214–222. <https://doi.org/10.1016/j.apcatb.2019.04.083>.

525 [45] C. Tan, T. Sheng, Q. Xu, T. Xu, K. Sun, L. Deng, W. Xu, Cobalt doped iron oxychloride as
526 efficient heterogeneous Fenton catalyst for degradation of paracetamol and phenacetin, *Chemosphere*
527 263 (2021). <https://doi.org/10.1016/j.chemosphere.2020.127989>.

528 [46] X. Gao, W. Peng, G. Tang, Q. Guo, Y. Luo, Highly efficient and visible-light-driven BiOCl for
529 photocatalytic degradation of carbamazepine, *Journal of Alloys & Compounds* 757 (2018) 455–465.

530 [47] J. Xu, L. Li, C. Guo, Y. Zhang, W. Meng, Photocatalytic degradation of carbamazepine by tailored
531 BiPO₄: Efficiency, intermediates and pathway, *Applied Catalysis B Environmental* 130-131 (2013)
532 285–292.

533 [48] Y.F. Rao, L. Qu, H. Yang, W. Chu, Degradation of carbamazepine by Fe(II)-activated persulfate
534 process, *JOURNAL OF HAZARDOUS MATERIALS* 268(mar.15) (2014) 23–32.

535

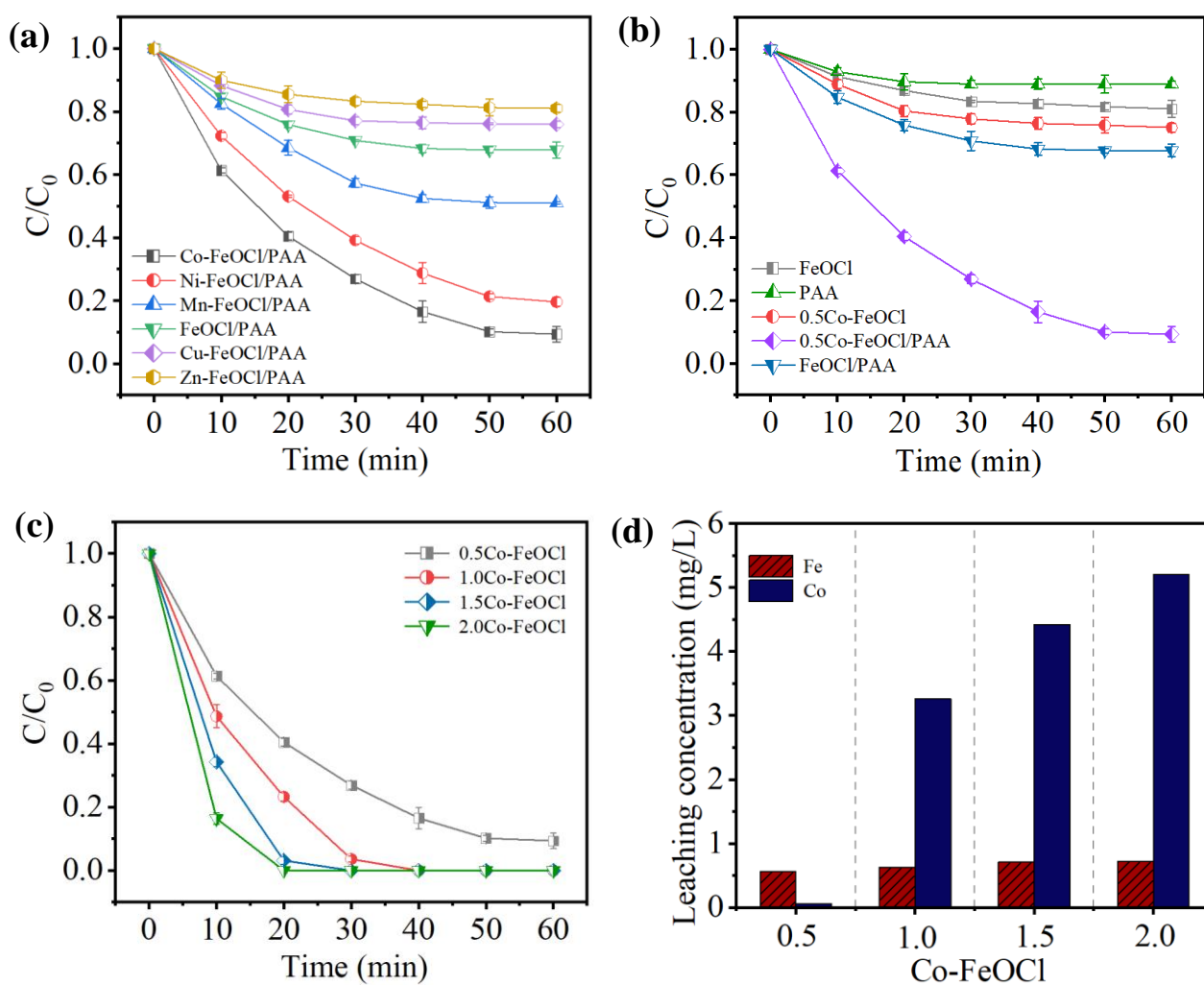


Figure 1. (a) CBZ removal by different metal-doped FeOCl (Co, Ni, Mn, Cu, Zn) in the presence of PAA; (b) CBZ removal by different systems; (c) the influence of Co doping level on the catalytic activity of Co-FeOCl and (d) corresponding Fe and Co ions leaching from different x Co-FeOCl. Reaction condition: [CBZ] = 10 μ M, [Catalyst] = 0.1 g/L, [PAA] = 0.6 mM, and without solution pH adjustment.

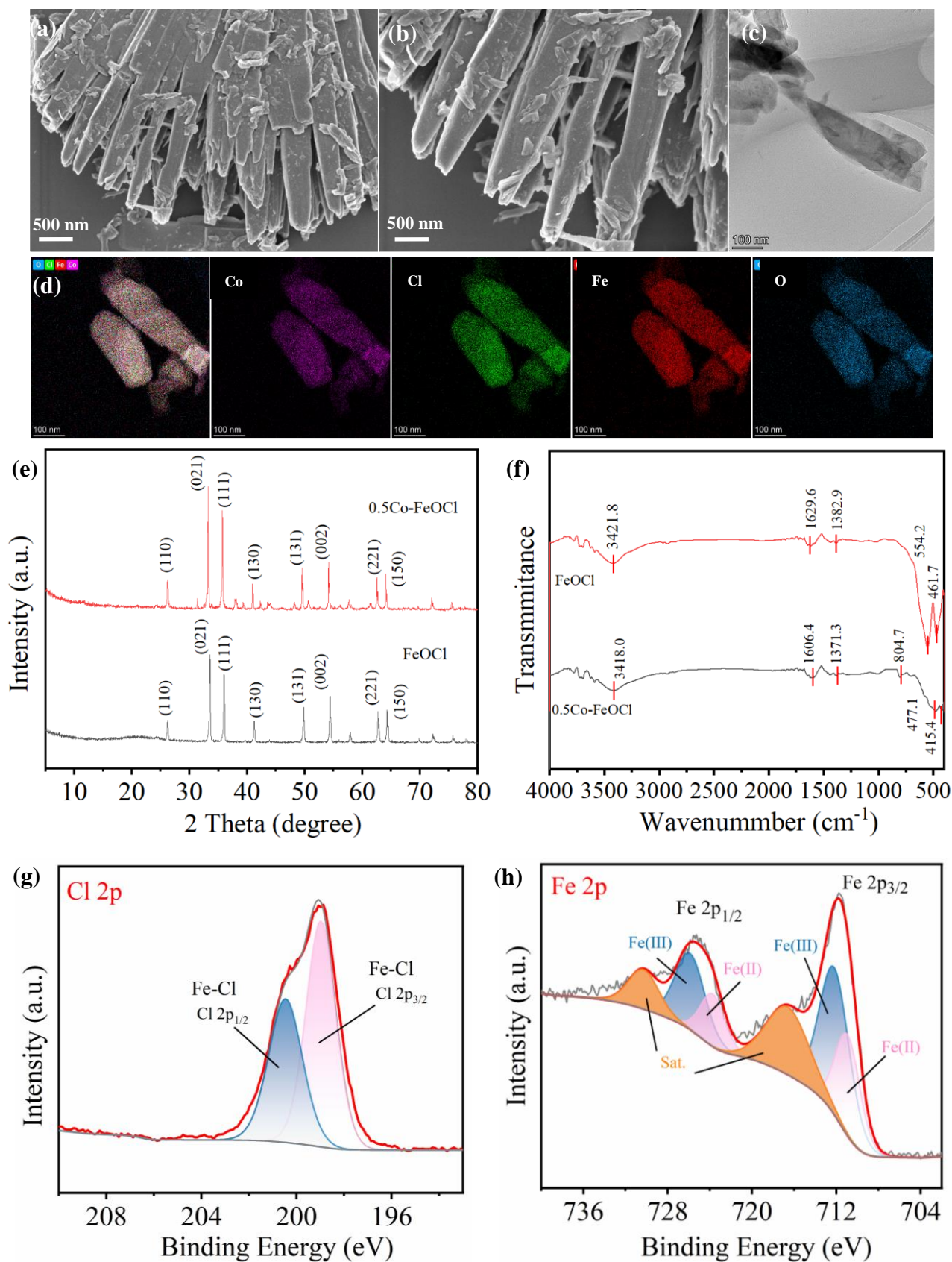


Figure 2. SEM images of (a) pristine FeOCl and (b) 0.5Co-FeOCl; (c) TEM image of 0.5Co-FeOCl; (d) EDS elemental mapping images of Co, Cl, Fe, and O in 0.5Co-FeOCl; (e) XRD patterns and (f) FTIR spectra of FeOCl and 0.5Co-FeOCl; XPS spectra of (g) Cl 2p and (h) Fe 2p in 0.5Co-FeOCl.

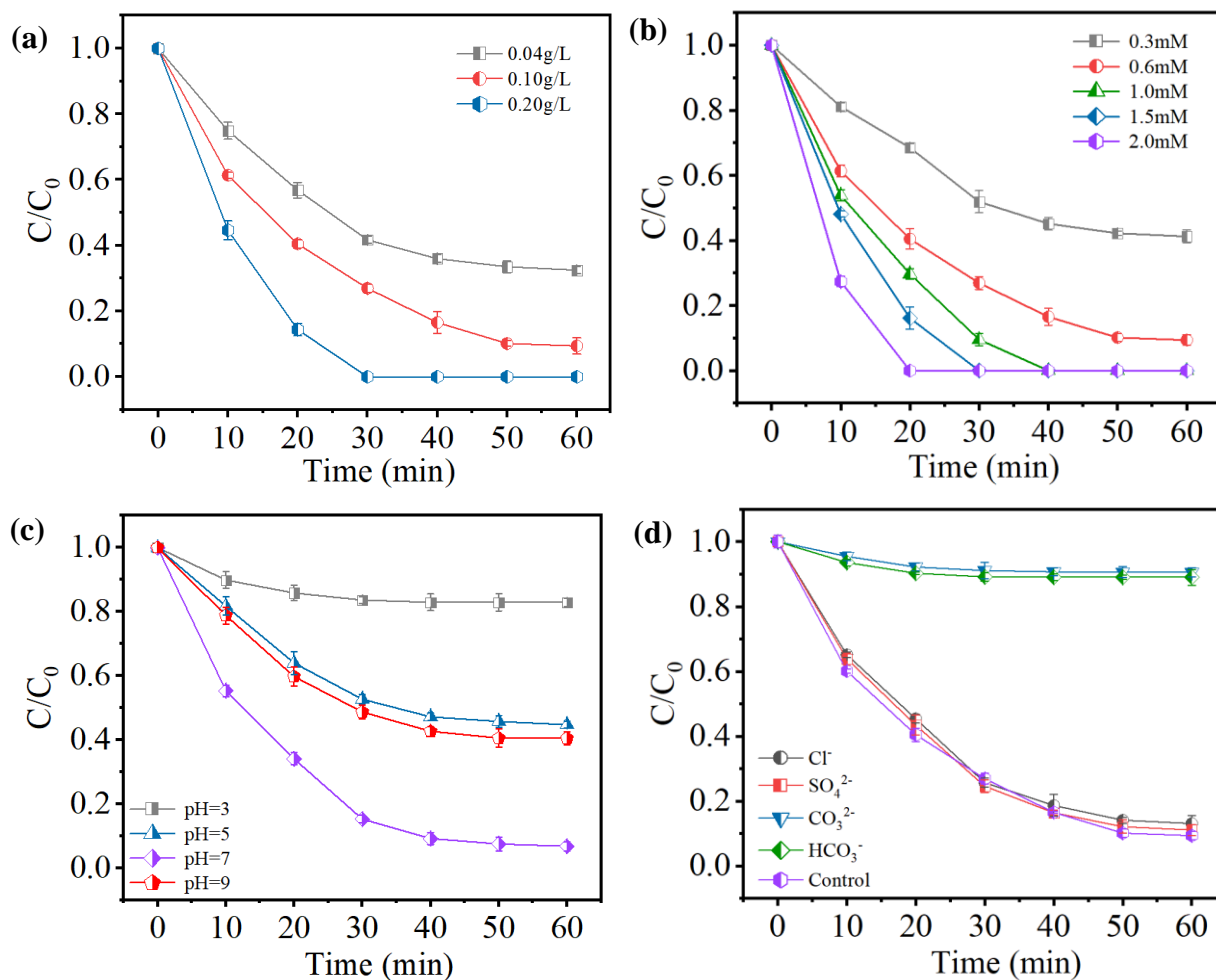


Figure 3. Effects of (a) 0.5Co-FeOCl dosage, (b) PAA concentration, (c) initial solution pH, and (d) common coexisting anions on CBZ removal in the 0.5Co-FeOCl/PAA system. Reaction conditions: unless otherwise noted, [CBZ] = 10 μM , [Catalyst] = 0.1 g/L, [PAA] = 0.6 mM, and without solution pH adjustment.

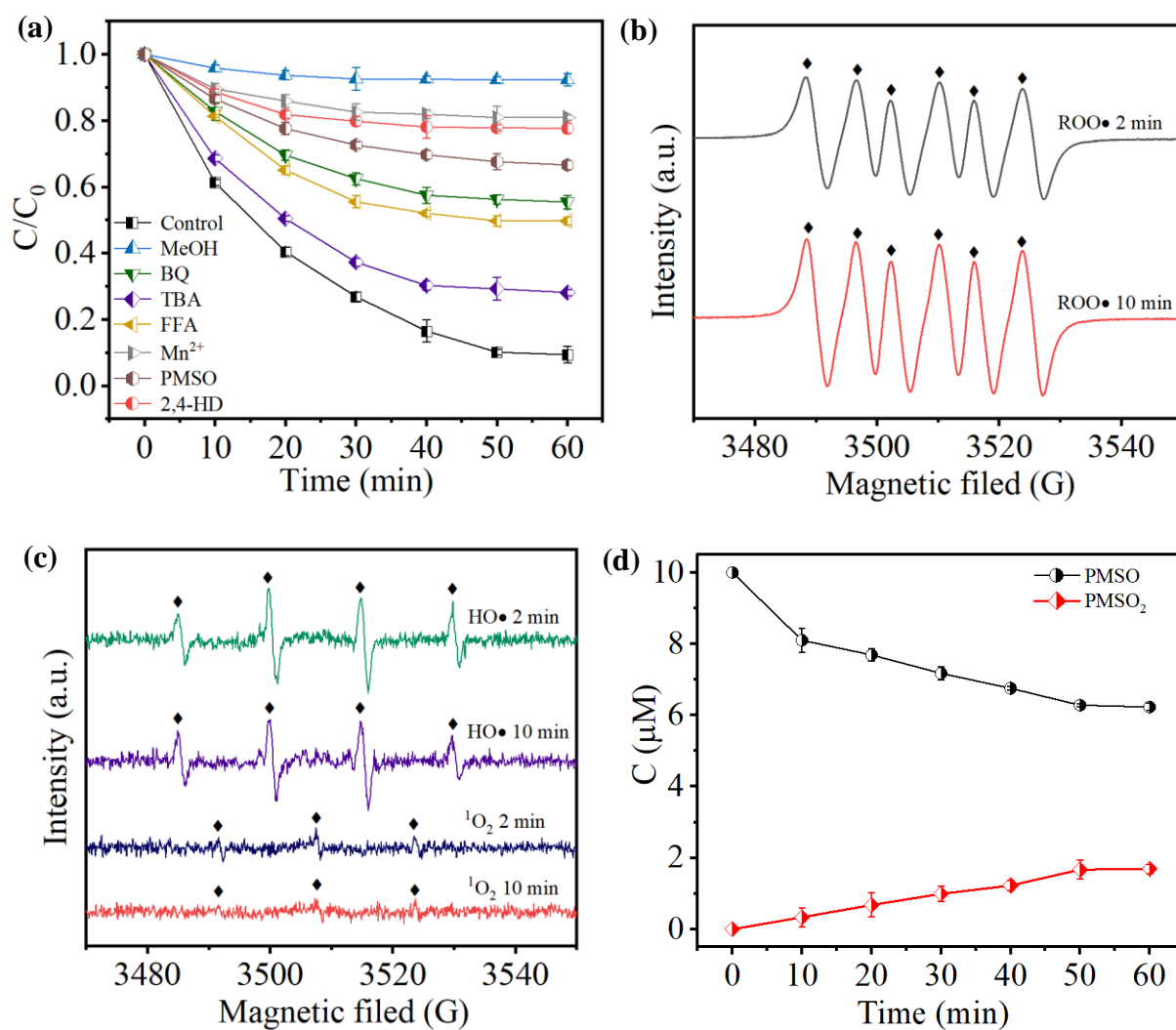


Figure 4. (a) The quenching tests using MeOH and TBA as scavengers ($[CBZ] = 10 \mu M$, $[Catalyst] = 0.1 \text{ g/L}$, $[PAA] = 0.6 \text{ mM}$, without pH adjustment, $[MeOH] = 50 \text{ mM}$, $[BQ] = 20 \text{ mM}$, $[TBA] = 50 \text{ mM}$, $[FFA] = 5 \text{ mM}$, $[Mn^{2+}] = 10 \text{ mM}$, $[PMSO] = 10 \mu M$, and $[2,4\text{-HD}] = 5 \text{ mM}$); EPR spectra of (b) DMPO-ROO•, (c) DMPO-•OH and TEMP- 1O_2 adducts; (d) PMSO consumption and PMSO₂ formation in the 0.5Co-FeOCl/PAA system.

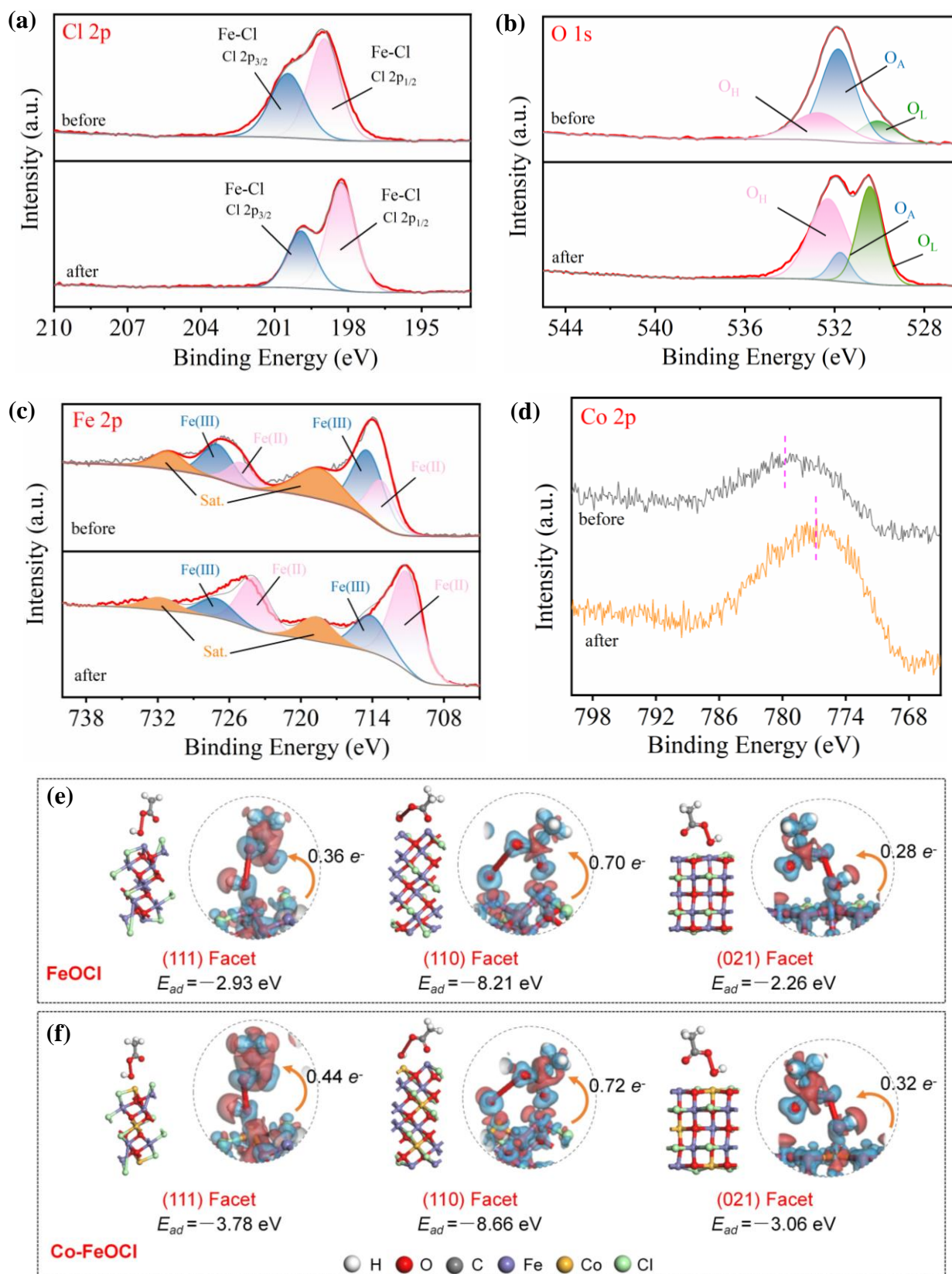


Figure 5. High-resolution XPS spectra of (a) Cl 2p, (b) O 1s, (c) Fe 2p, and (d) Co 2p in 0.5Co-FeOCl before and after the catalytic reaction. Optimized adsorption conformations and charge density difference of PAA on the (111), (110) and (021) facets of (e) FeOCl (f) and Co-FeOCl. Red and blue contours represent electron deletion and accumulation, respectively.

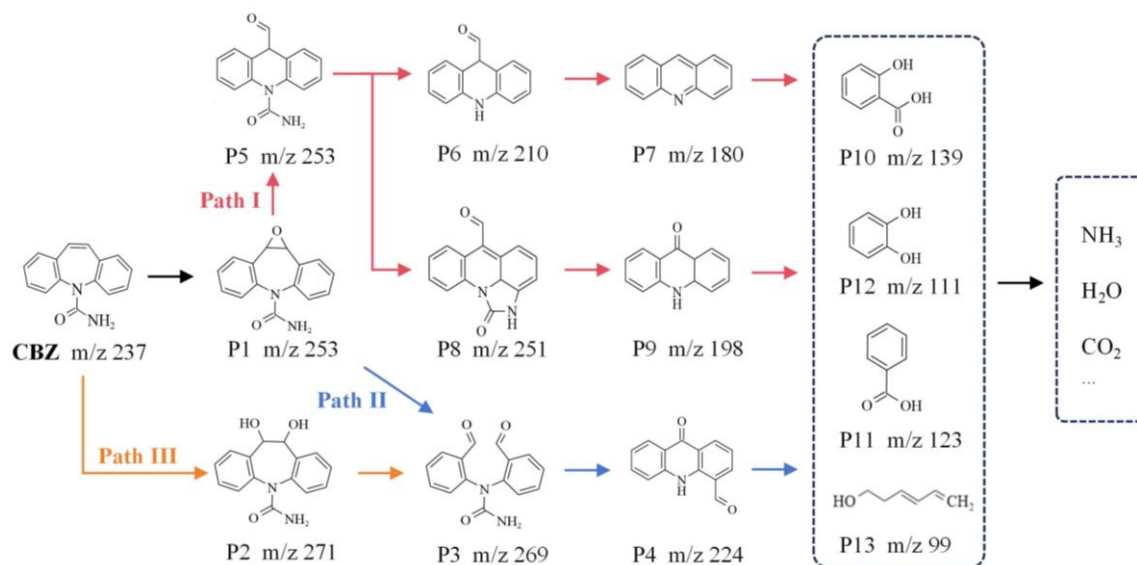


Figure 6. The possible degradation pathway of CBZ in the 0.5Co-FeOCl/PAA system.

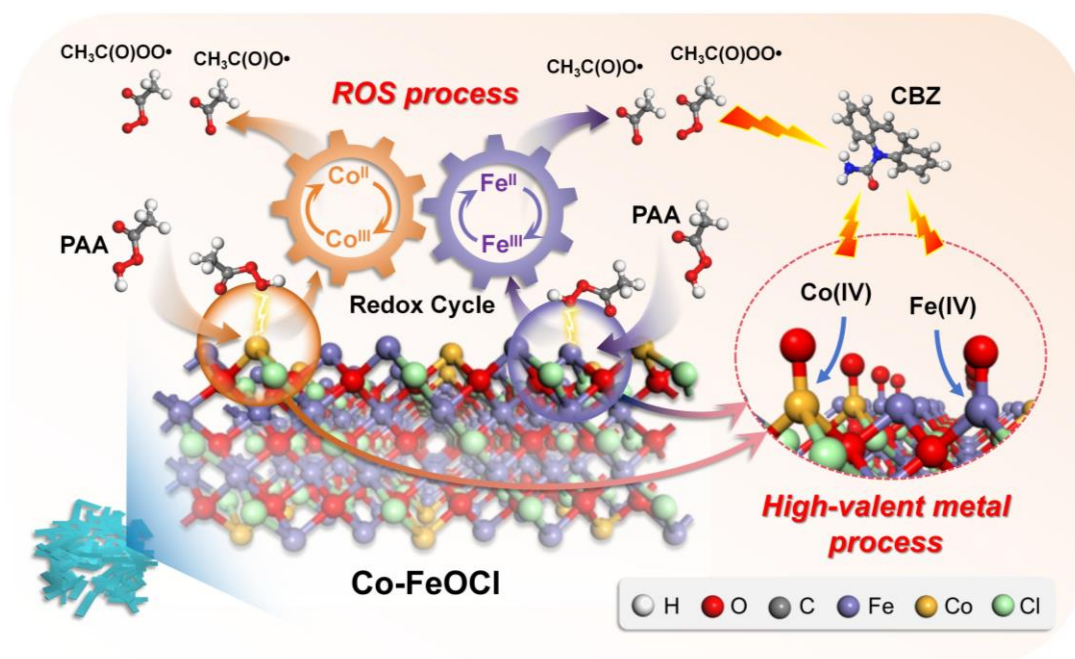
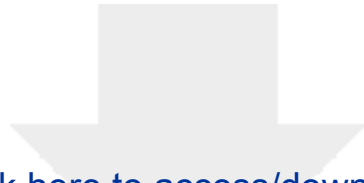
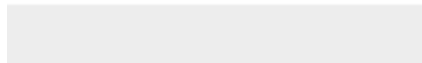


Figure 7. The proposed organic radicals and high-valent metals dominated mechanisms for CBZ degradation in the Co-FeOCl/PAA system.



Click here to access/download
Supplementary Material
Supplementary Material.doc



Declaration of interests

The authors declare that they have no known competing financial interests or personal relationships that could have appeared to influence the work reported in this paper.

The authors declare the following financial interests/personal relationships which may be considered as potential competing interests: